Numerical study on the evolution of surface defects in wire drawing

Hyun Moo Baek [a], Young Gwan Jin [b], Sun Kwang Hwang [a], Yong-Taek Im [a,*], Il-Heon Son [c], Duk-Lak Lee [c]

[a] National Research Laboratory for Computer Aided Materials Processing, Department of Mechanical Engineering, KAIST, 291 Daehak-ro, Yuseong-gu, Daejeon 305-701, Republic of Korea
[b] PIE & Radwaste Division, KAERI, 1045 Daedeok-daero, Yuseong-gu, Daejeon 305-353, Republic of Korea
[c] Wire Rod Research Group, Technical Research Laboratories, POSCO, 1 Goedong-dong, Nam-gu, Pohang, Gyeongbuk 790-785, Republic of Korea

ABSTRACT

In this study, a three-dimensional finite element analysis for multi- or single-pass wire drawing was carried out in order to evaluate the deformation behavior of various surface defects, such as longitudinal, transverse, oblique, and round, introduced during the manufacturing processes. For numerical simulations, a free surface contact treatment algorithm was employed to suppress node penetration by applying a penalty method. Simulation results were compared with the experimental data obtained by optical microscopy for multi-pass drawing samples of the medium carbon steel wire with a longitudinal round-type defect in terms of variation of the load requirement and evolution of the cross-sectional shape of the surface defect. Additional numerical studies were carried out to investigate changes of cross-sectional shapes of various surface defects depending on stress distributions in the single-pass wire drawing. It was found that the radial and circumferential stress components determined the final shape and aspect ratio of the defect. The current numerical approach can be helpful in determining a guideline to assess the acceptability of the surface quality of the drawn wire for the secondary manufacturing process based on the available data in the literature.

© 2011 Elsevier B.V. All rights reserved.

1. Introduction

Surface quality assurance of hot rolled wires is important because surface defects can develop into an external burst in the forged products during a secondary process of manufacturing, accounting for roughly 50% of raw material rejections, as reported by Huang et al. (2004). It is widely known that the occurrence, propagation, and disappearance of surface defects involved with producing the wires are not yet fully understood because of the complexity of many production stages in casting, hot rolling, and transportation, as well as the difficulty of the measurements during the process. Sychkov et al. (2006) attempted to classify various types of surface defects in the wires transformed from the steel-making process. They pointed out that an accurate classification of surface defects on the rolled products was not easy.

In the forging industry, single- or multi-pass wire drawing might be applied to reduce the diameter of the material in addition to improving its surface and mechanical quality. Owing to such complexities involved with the wire productions, the acceptable standard for surface defects is described in the ASTM Standard (F2282-03, 2009).

In order to better understand the forming mechanism of a surface defect, the hot bar rolling process was studied by Kwon et al. (2009) by applying the finite element (FE) analysis in conjunction with a conventional plastic work approach. According to their results, the surface defect was identified as a wrinkle defect occurring at an earlier stage of a roughing mill, and recrystallization further affected the instability of the deformation in the wire during the manufacturing process. They also reported that temperature and specific deformation energy levels governed the occurrence of the wrinkle defect, although the specific deformation level was dependent on the roll geometry. Based on the measured compression data, Kim et al. (2008) derived processing maps and applied them to the prediction of the surface defect formation observed in industry. Lee et al. (2007, 2008) and Awais et al. (2008) found that less flow instability was observed by increasing the initial rolling temperature whereas it was less sensitive to the change of the roll geometry introduced at each pass. On the other hand, Son et al. (2008) investigated the deformation behavior of surface defects with a notched shape on the billet in the multi-pass hot rolling process using the FE code, CAMP*roll*, developed by Kim et al. (2005). They focused on numerical study in which intentionally introduced notches on the billet can either diminish or grow depending on their initial sizes and locations. In spite of these efforts, the phenomenon
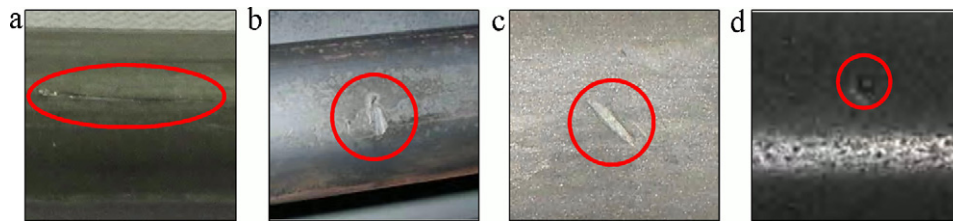
Fig. 1. Various types of surface defects observed in production: (a) longitudinal, (b) transverse, (c) oblique, and (d) round defect.

is not quite well understood yet, and it is almost impossible to perfectly prevent or remove the surface defect involved with various processing conditions due to a number of unknown sources.

In a steel bar and wire production, the drawing process is normally introduced after rolling to reduce the diameter of the wire by pulling it through a single or series of drawing dies. During wire drawing, the surface defects transformed from the rolling process could survive or diminish depending on the processing condition. In industry-related applications, cutting or grinding might be necessary to remove such surface defects before wire drawing because the drawn wire can be used as both a final product and a source material for subsequent manufacturing like forging.

A study on the deformation behavior of the surface defect during the wire drawing process was carried out by Yoshida and Shinohara (2004). They found that a deep transverse crack on the wire surface may develop into a defect known as a check-mark during repeated drawing passes. Shinohara and Yoshida (2005a) also studied the wire drawing of a bar containing an initial longitudinal defect with a rectangular cross-section by using the FE analysis. The results indicated that the defect was closed at the bar surface after the second pass, but an internal overlap with the shape of an "inverted Y" remained in the workpiece. In addition, Shinohara and Yoshida (2005b) analyzed the evolution of the V-notched longitudinal defect introduced in stainless steel during the wire drawing. They showed that larger notch angles, a larger semi-die angle, and a reduction of area (RA) per pass led to a larger decrease in the depth of the defect. However, the final product almost displayed defects with an overlap in its root and an opening at the bar surface.

As mentioned earlier, there are various types of surface defects on the wire in terms of their cross-sectional shape and direction, as shown in Fig. 1. In the steel mill, it is necessary to set up a guideline to determine the acceptability of the hot rolled wire depending on

the evolution of the various surface defects as given in the ASTM Standard (F2282-03, 2009). In this regard, limited research have been undertaken to predict the evolution of surface defects due to the difficulties of the contact treatment algorithm of the free surfaces in the FE analysis and measurement of surface defects during the process.

In this study, arbitrary surface defects were introduced in the initial workpiece and the evolution of deformation behavior of such defects was numerically simulated during the multi-pass wire drawing. The wire drawing experiments were carried out to verify numerical simulations for the longitudinal round-type surface defect model for the medium carbon steel specimen. Numerical simulations were further extended to investigate various directional and cross-sectional changes of surface defects for a single-pass drawing depending on the radial and circumferential stress distributions. Finally, the deformed geometry was assessed based on the final depth and aspect ratio of the surface defects to determine the available guideline that can be employed to check the applicability of the present approach for assessing the acceptability of the produced wires for a secondary process.

2. Experimental

The cross-section of the surface defect on the wire, as shown in Fig. 1(a), was assumed to be a round shape, according to the work by Kwon et al. (2009), and artificially introduced on the steel wire in the longitudinal direction, as shown in Fig. 2. In this figure the width w and the depth d of the surface defect are defined, and the aspect ratio φ is introduced as w/d for determining geometrical changes of various surface defects investigated in the present study. The dimension of the initial width and depth of the longitudinal round-type defect introduced for the multi-pass drawing
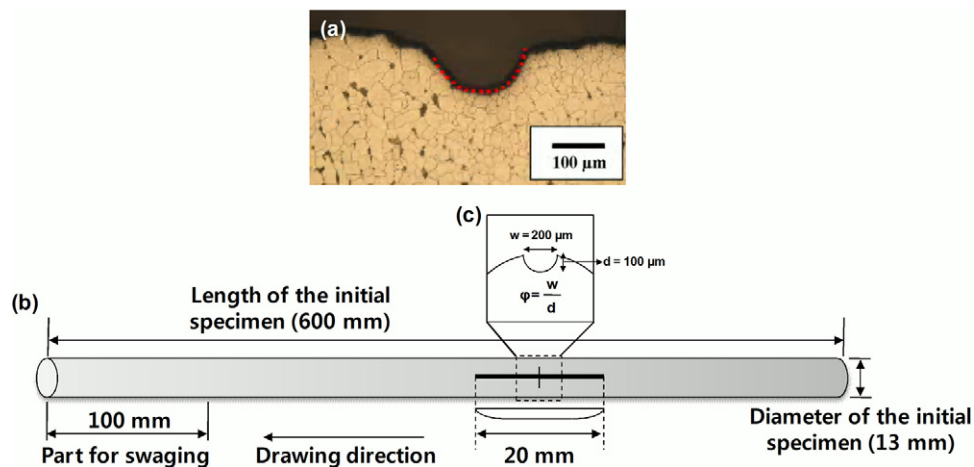

Fig. 2. Schematic diagram of the initial surface defect and specimen: (a) surface defect represented in the literature (Kwon et al., 2009), (b) the specimen with an artificially introduced longitudinal round-type defect, and (c) a cross-sectional view of the round-type defect.

Table 1
Chemical composition of SWRCH45K (wt.%).

Material	C	Si	Mn	P	S
SWRCH45K	0.453	0.225	0.754	0.024	0.028

Table 2
Process parameters of the drawing dies used for the multi-pass drawing of the longitudinal round-type surface defect.

No. of passes	Semi-die angle (°)	Diameter (mm)	Bearing length (mm)
First	6	11.6	3.5
Second	6	10.4	3.1
Third	6	9.3	2.8

were 200 and 100 μm, respectively. In the present investigation, the commercially available medium carbon steel SWRCH45K (JIS G3507) was used, and its chemical composition is given in Table 1.

To check the validity of numerical simulations, a multi-pass wire drawing of the specimen with the longitudinal round-type surface defect was carried out. The diameter and length of the initial specimen for the multi-pass drawing were 13 and 600 mm, respectively. A constant drawing velocity of 16.67 mm/s was used for the experiment at room temperature, and a commercially available solid lubricant whose main component is MoS_2 was applied to the specimen in the experiments. The experiment was conducted using a draw bench available at the POSCO Technical Research Laboratory for three passes with the prepared specimen to investigate the deformation behavior of the artificially introduced surface defect.

The drawing dies were made of commercially available tungsten carbide, and the internal geometry of the dies was a conical type. Table 2 shows the geometrical process parameters of the drawing dies for the multi-pass drawing. The RA described in Eq. (1) was 20% for each pass for the multi-pass wire drawing.

$$\text{RA} \ (\%) = \frac{A_o - A_f}{A_o} \times 100,$$ (1)

where A_o and A_f refer to the initial and final cross-sectional area, respectively.

To investigate the variation of the cross-section of the surface defect, each specimen was sectioned at the central part of the defect in the drawing direction. The specimens were polished by SiC paper and diamond suspensions of up to 1 μm for the cross-section. The prepared samples were observed by optical microscopy at 200× magnification. The width and depth of the deformed defects were measured by applying the image measurement program.

The material property of the specimen used for the FE analysis was obtained from the simple tension test according to the ASTM Standard (E8M-04, 2006). The tension specimens of 5 mm in diameter with a gauge length of 25 mm were used for the tests. To check the strain rate effect of the material, the tests were conducted three times for each test with a universal testing machine (Instron 4206) using two constant testing velocities of 0.0167 and 1.67 mm/s, which correspond to initial strain rates of 6.7×10^{-4} and $6.7 \times 10^{-2} \ s^{-1}$, respectively, at room temperature. During the tension tests, elongation was measured by a mechanical extensometer (Instron 2630-100 series clip-on type, USA) with a gauge length of 25 mm and a travel of −2.5 to +25 mm. The strain rate effect was not influential in the test results, and, as shown in Fig. 3, the stress–strain curve of specimen 3 measured with a constant testing velocity of 0.0167 mm/s was fitted as a power law. Since a necking phenomenon was observed at a strain of approximately 0.03 in this
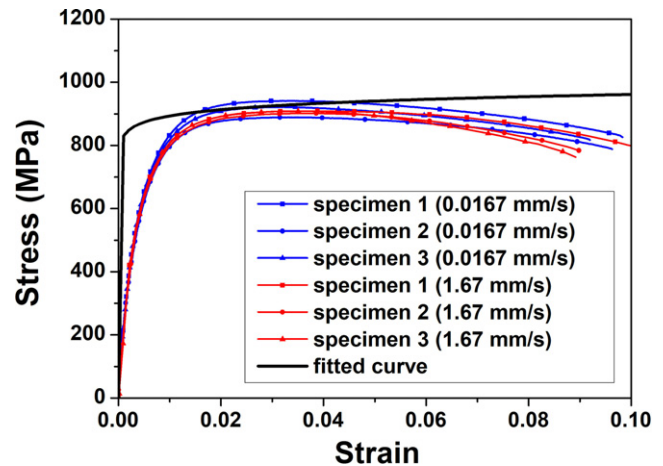

Fig. 3. Fitted flow stress–strain curve obtained from the tension test.

figure, the flow stress curve was fitted to Eq. (2) using the measured data for numerical simulations:

$$\sigma = K\varepsilon^n(K = 1035 \ \text{MPa}, \quad n = 0.032),$$ (2)

where σ and ε refer to the flow stress and strain, respectively.

3. Numerical

Chen and Kobayashi (1978) applied the rigid-viscoplastic approach for the analysis of the wire drawing process for the first time. In the present study, an in-house FE program, CAMP*form*3D, developed by Kim and Im (2002) to analyze a bulk metal forming process based on a rigid-viscoplastic constitutive model by adopting three-dimensional auto remeshing schemes introduced by Kwak and Im (2002), was used to simulate the multi- or single-pass wire drawing of the hot rolled wire containing artificially introduced surface defects.

In numerical simulations, the dies were considered to be rigid and the workpiece was pulled along the drawing direction using sticking condition between the grip and workpiece. Table 3 shows the detailed analysis conditions used for numerical simulations. In order to simulate the steady state behavior of the surface defect during the wire drawing, the minimum length of the initial workpiece was chosen to minimize the calculation time. To reduce the oscillation of the predicted forming loads, the density of the mesh system was increased along the drawing direction, similar to the work by Chevalier (1992). To apply a frictional force at the interface between the specimen and the drawing die, the constant shear friction model with a shear friction factor of $m_f = 0.1$ was used in simulations according to the literature (Altan et al., 1983). In the present investigation, the numerical simulation was carried out in the Cartesian coordinate system while the stress distributions were transformed into the cylindrical coordinate system by post-processing since the wire drawing process might usually be under an axisymmetric condition.

3.1. Multi-pass wire drawing of the longitudinal surface defect

Because of the geometrical symmetry of the specimen, a half-symmetric FE model using brick elements was used for the numerical analysis for the longitudinal round-type defect, as shown in Fig. 4. Finer mesh was also used near the surface defect because of localized severe deformation in the vicinity of the surface defect. Along the drawing direction, a refined mesh layout was adopted in the middle of the workpiece, where the shape and stress distributions were closely monitored. A constant drawing velocity used in

Table 3
Analysis conditions for the numerical simulations.

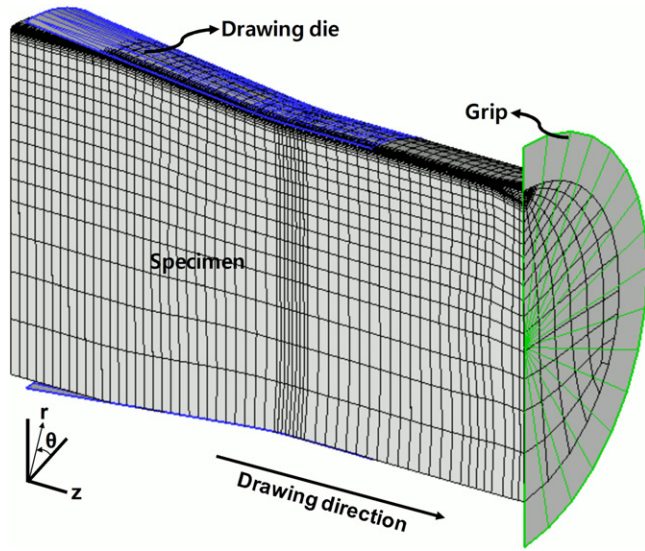| No. of simulation	Diameter of the initial specimen (mm)	Length of the initial specimen (mm)	No. of element	Drawing velocity (mm/s)
Multi-pass simulation	13	25	6880	16.67
Single-pass simulation	8	15	3773	28.33

Fig. 4. Finite element model used for simulations.

the numerical simulation was the same as that of the experiment: 16.67 mm/s.

3.2. Single-pass wire drawing of the various surface defects

Three types of cross-sectional shapes, namely, sharp, medium, and blunt surface defects, were introduced in simulations to mimic the surface defects, as given in Fig. 1. The initial depth for these kinds of defects was assumed to be 100 μm according to the work by Imiya et al. (1981). The initial widths were varied to be 100, 200, and 300 μm.

The cross-sectional shape of each case (y) was assumed to be a parabolic shape as given in Eq. (3) for a single-pass wire drawing in the present numerical simulations,

$$y = d \left| \frac{x}{0.5w} \right|^{\beta}, \tag{3}$$

where w, d, and β are the initial width, initial depth, and shape parameter in that order. Depending on the condition of β, Eq. (3) can describe the various cross-sectional shapes of the surface defect. In the case of $\beta = 1$, the cross-section represents the triangular shape while it asymptotically represents the rectangular shape as β approaches infinity.

In Fig. 5, the surface defects are plotted for the case of $\beta = 2$ in the range of $-0.5w \leq x \leq 0.5w$ with $w = 100, 200, 300$ μm and $d = 100$ μm. The aspect ratio φ in this figure was defined in Fig. 2. It is shown in Fig. 5 that the type of surface defect can be uniquely determined by the given aspect ratio. Depending on the geometrical symmetry of the surface defect, a half or full model of the analysis was adopted in the simulation.

3.3. Free surface contact algorithm

When free surface folding occurs in the metal forming simulation, contact treatment between free surfaces should be handled properly because the free surfaces facing each other will penetrate
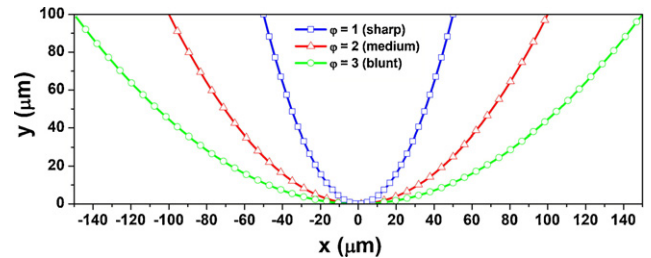

Fig. 5. Various cross-sectional shapes of the surface defect defined by Eq. (3) depending on the aspect ratio φ.

if the contact problem is not carefully treated. In the current study, the self-contact searching and constraint algorithms developed by Hahn and Im (1995) for the simulation of the two-dimensional folding phenomenon were adopted and revised for the analysis of a three-dimensional wire drawing of a hot rolled wire containing surface defects.

For contact treatment between free surfaces, contacting nodes must first be identified during simulations. First, a free surface node was prescribed as a slave node while the remaining free surface nodes were defined to be master nodes, as introduced in Fig. 6. Then, the normal distances between this slave node and all master segments in this figure can be calculated. If this distance (l) was within a specified tolerance, $l_{tol} = 0.001$, this node was determined to be a possible contact node. This process was repeated for all free surface nodes to determine possible contacting nodes.

Once all contacting nodes were identified, a proper boundary conditions needed to be applied in order to prevent penetration between contacting free surfaces. To enforce the impenetration condition, the penalty method was introduced. In this regard, a constraint contact force depending on the amount of relative velocity was calculated as follows:

$$\int_{\Gamma} \mathbf{F}_n \delta \mathbf{v_i} \, d\Gamma = \int_{\Gamma} \alpha (\mathbf{v_i} - \mathbf{v_{ic}}) \delta \mathbf{v_i} \, d\Gamma, \tag{4}$$
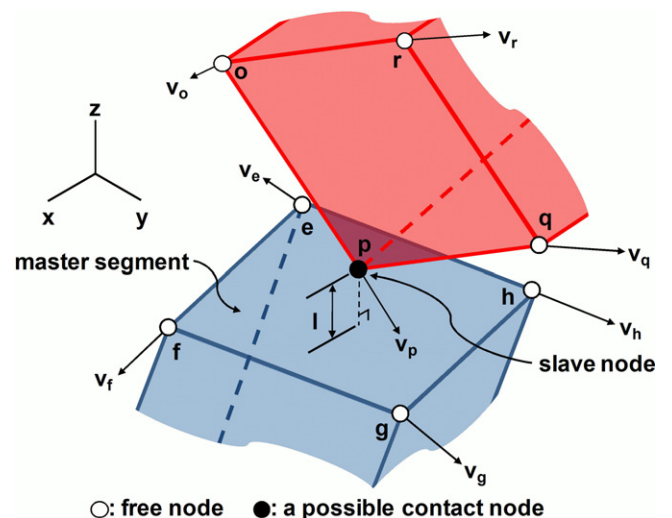

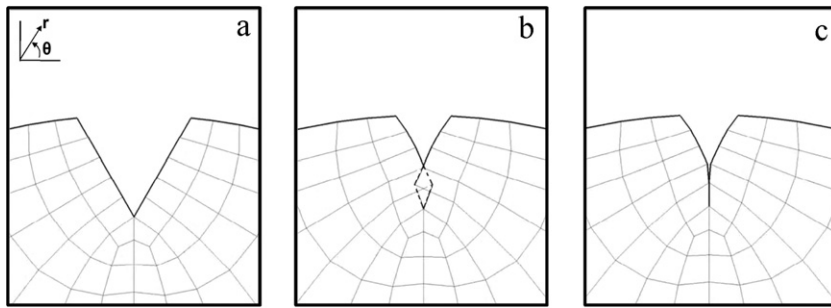**Fig. 6.** Schematic diagram of the free surface contact treatment.

Fig. 7. Implementation of the self-contact algorithm: (a) initial, (b) before, and (c) after the contact treatment.

where $\mathbf{v_i}$, $\mathbf{v_{ic}}$, α, and Γ are the nodal velocity, velocity of the contacting node, penalty constant, and contacting area, in that order. This weak form was added to the traction boundary term obtained from the finite element formulation of the equilibrium equation.

In the present investigation, the impenetration condition was satisfied by assuming the rigid body motion of any contacting node or nodal points in the contact region, as shown in Fig. 6. Therefore, the nodal velocity in the contact region was calculated by Eq. (5) from the nodal velocities of the contacting node and segment in the same figure.

$$\mathbf{v_{ic}} = \mathbf{v_{cx}} + \mathbf{v_{cy}} + \mathbf{v_{cz}},$$

where

$$\mathbf{v_{cx}} = [\{(v_{ex} + v_{fx} + v_{gx} + v_{hx})/4\} + v_{px}]/2 .$$ (5)

$$\mathbf{v_{cy}} = [\{(v_{ey} + v_{fy} + v_{gy} + v_{hy})/4\} + v_{py}]/2$$

$$\mathbf{v_{cz}} = [\{(v_{ez} + v_{fz} + v_{gz} + v_{hz})/4\} + v_{pz}]/2$$

Fig. 7 shows the results of simulations of the longitudinal surface defect with a V-notched cross-section without and with applying the contact treatment algorithm for free surface folding. Fig. 7(c) shows that the penetration between free surfaces was prevented with the application of the current algorithm.

4. Results and discussion

4.1. Multi-pass wire drawing of the longitudinal round-type surface defect

The numerical and experimental load-stroke curves obtained from the multi-pass wire drawing of the longitudinal surface defect are compared in Fig. 8. There are small discrepancies at the earlier deformation stage in this figure because of an irregular swaging part in the specimen during load measurements in the experiment. However, the simulated load values with m_f = 0.1 were generally in
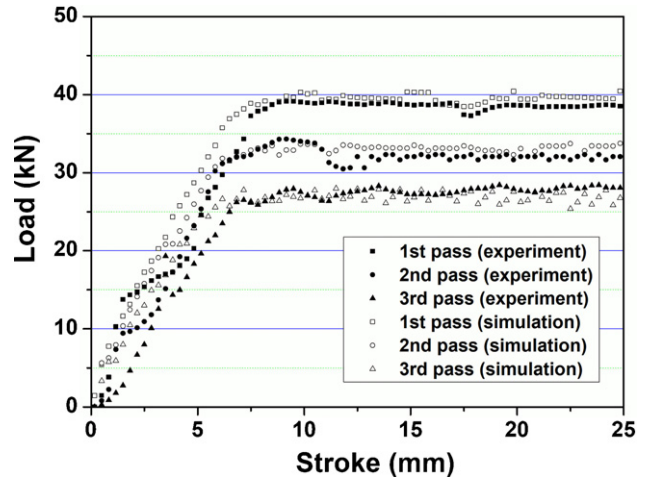

Fig. 8. Experimental and numerical load requirements for the multi-pass wire drawing of the longitudinal round-type surface defect.

good agreement with the measured values for the steady state of the multi-pass wire drawing. Therefore, the shear friction factor of m_f = 0.1 was assumed to be a reasonable value for the analyses of the multi-pass wire drawing process under the present investigation conditions.

Deformed specimens obtained from the experimental and numerical results for three passes are shown in Fig. 9. Even though slight differences between the experimental and numerical results are observed in this figure, the numerical simulation reproduced the deformed configuration of the surface defect in the multi-pass wire drawing reasonably well. According to the present result, the cross-sectional shape of the longitudinal round-type surface defect was maintained to be similar to the original cross-sectional shape
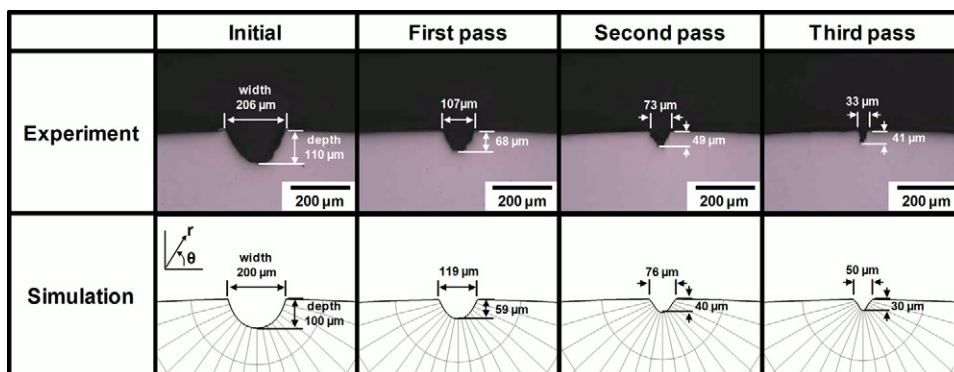

Fig. 9. Comparison of deformed shapes of surface defects obtained from the experiment and simulation.
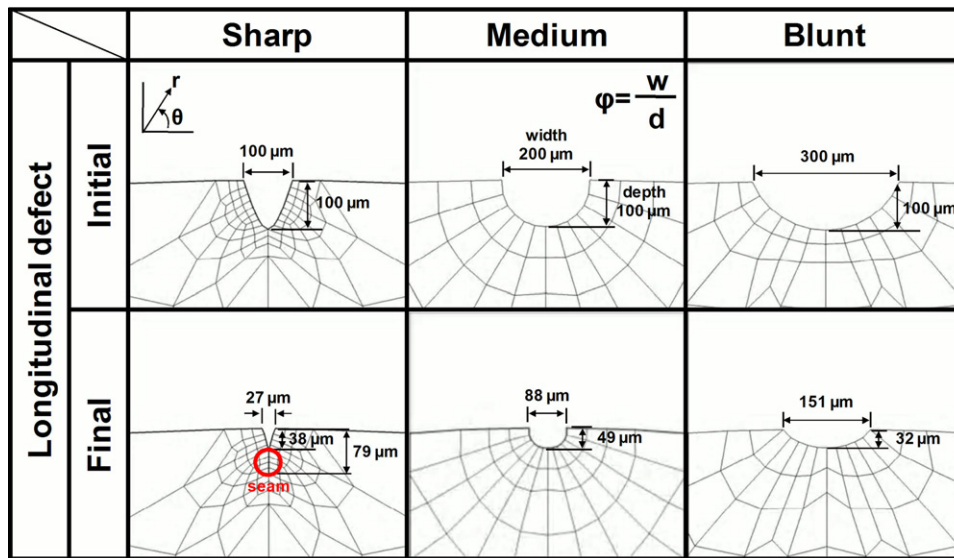
Fig. 10. Deformed shapes of the longitudinal surface defects after the single-pass wire drawing.

during the multi-pass wire drawing even though its width and depth dimensions were changed.

In addition, this figure shows variations of the width and depth of the surface defect in three passes of the wire drawing according to the experiment and simulation. Geometrical variations also showed a reasonably similar pattern between the experiment and simulation.

4.2. Simulations of single-pass wire drawing of various surface defects

Since the FE analysis could predict a longitudinal round-type surface defect evolution in the wire drawing reasonably well, this approach could be further extended to investigate other types of defects such as transverse, oblique to the drawing direction by 60°, and round defects. For simulations, a single-pass wire drawing was applied owing to the prior simulation results in which the surface defects were significantly deformed at the first pass of the multi-pass wire drawing. General drawing conditions of semi-die angle (7°) and RA (20%) were used in simulations, and the other simulation conditions were the same as in the multi-pass simulation. As mentioned earlier, numerical simulation of the single-pass wire drawing with the oblique defect was conducted using a full FE model while the initial and final shape of this defect was expressed as a half model similar to the cases for the transverse and round defect for better representation.

Fig. 10 shows the deformed shapes of the longitudinal surface defects after the single-pass wire drawing. In the case of a sharp cross-section with an initial aspect ratio of unity (initial $\varphi = 1$), the defect evolved into an overlapped defect called a seam. The aspect ratio φ was defined as the ratio of the width to the depth of the surface defect, as introduced in Fig. 2. In such a case of the overlapped defect, it might be confusing to assess the surface quality because the depth of the overlapped defect cannot be easily measured. Therefore, the longitudinal defect with the sharp cross-sectional shape should be eliminated before the wire drawing to obtain a better surface quality of the drawn wire. On the other hand, a medium cross-section (initial $\varphi = 2$) was deformed, similar to the original shape, even though its width and depth were decreased. In the case of a blunt cross-section (initial $\varphi = 3$), the surface defect seemed to

be diminished after the wire drawing since it was changed into a shallow groove.

The deformed shapes of transverse, oblique, and round defects are shown in Fig. 11. The transverse defect was formed on the surface of the wire in perpendicular to the drawing direction, and the initial cross-sectional shape was changed into a similar or shallower shape after the wire drawing. In this case, the initial cross-sectional shape was not changed into the overlapped defect after one-pass drawing even though it was sharp. The oblique defect easily found in the production line showed intermediate deformation behavior between the longitudinal and transverse defects. Since the defect was stretched and rotated along the drawing direction, as shown in this figure, the oblique defect seemed to represent the deformation behavior of the longitudinal surface defect in the subsequent wire drawing process.

In the current study, the round defect was assumed to be elliptic and the aspect ratio, $\varphi = w/d$ (introduced in Fig. 2), of this defect was assumed to be equal to or larger than 2. After the single-pass wire drawing, the shape of the round defect was changed into an oval shape because it was stretched along the drawing direction like the transverse or oblique defect. In the subsequent wire drawing process, the round defect seemed to deform like the longitudinal defect.

Table 4 shows the changes of the width, depth, and aspect ratio after the single-pass wire drawing. The width and depth of the surface defect were measured using the nodal information of the cross-section obtained from each simulation. For most of the simulation cases, except for the round case, the widths of surface defects decreased compared to the one of the initial defect, as shown in this table. On the other hand, the final depth decreased compared to the one of the initial defect, regardless of their directions and cross-sections. The transverse defect was particularly easy to diminish compared to other directions in terms of the decreased amount of the depth. The aspect ratios for most cases increased after the single-pass wire drawing, except for the longitudinal direction of the sharp and medium cross-sections. The increased amount of the aspect ratios of the longitudinal defect of the blunt cross-section was smaller than those of the transverse and oblique directions, which means that the longitudinal defects were difficult to cure after the wire drawing process compared to the other directions. In case of the longitudinal defect with a sharp
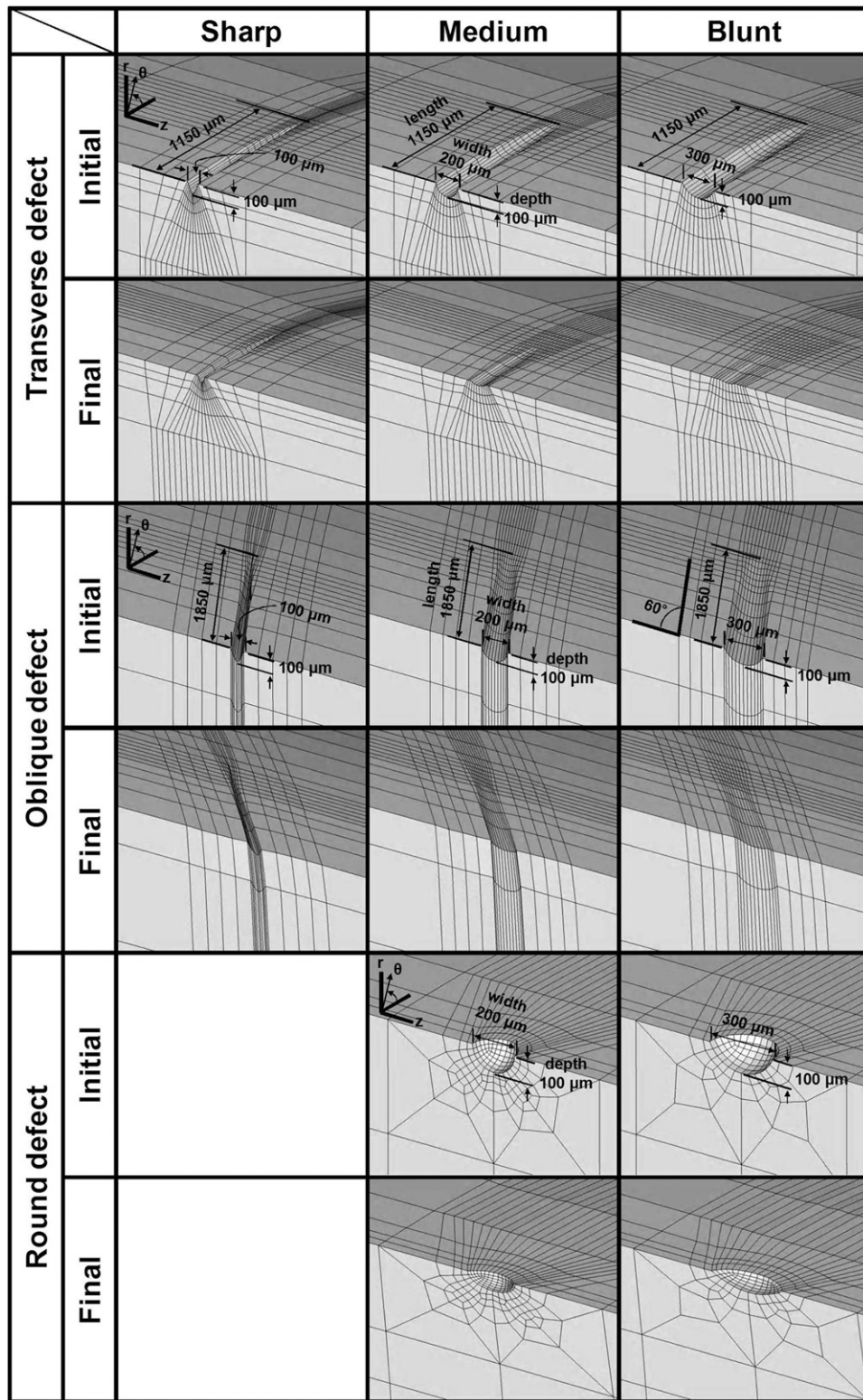
Fig. 11. Deformed shapes of the transverse, oblique, and round surface defects.

cross-sectional shape, the aspect ratio considerably decreased after the wire drawing because the defect was overlapped.
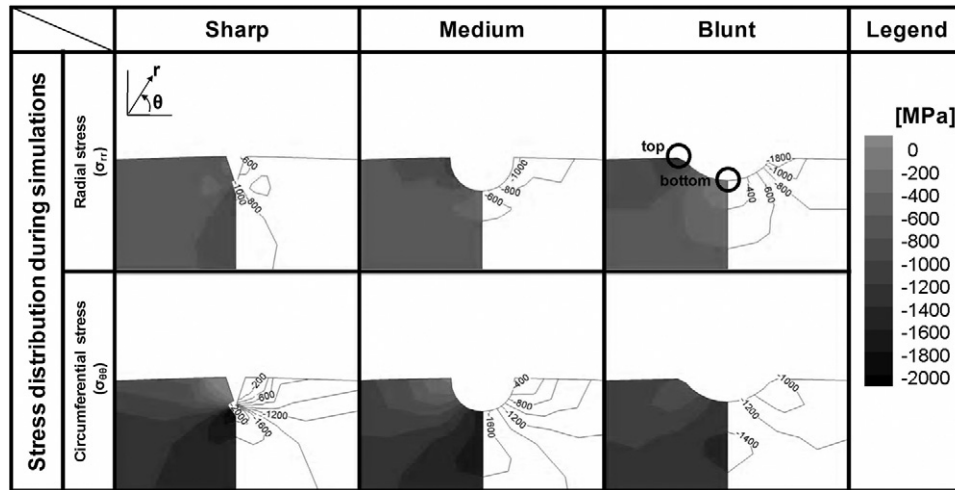
The stress distributions of the longitudinal defects are shown in Fig. 12. In this figure, the stress concentration and distribution were mainly dependent on the initial shape of the defect, even though the direction of the surface defect was the same. Since the final shape of longitudinal surface defect was affected by the stress

distribution during the wire drawing, the circumferential ($\sigma_{\theta\theta}$) and radial stress (σ_{rr}) components at the top and bottom of the surface defects, respectively, are compared. In case of the sharp cross-section, the circumferential stress component at the top and the radial stress component at the bottom were −200 and −1000 MPa, respectively. The circumferential stress component made the surface crack overlap after the wire drawing while the change of the

Table 4
Changes of the various surface defects after the single-pass wire drawing.

Direction		Longitudinal			Transverse			Oblique			Round	
Cross-section		Sharp	Medium	Blunt	Sharp	Medium	Blunt	Sharp	Medium	Blunt	Medium	Blunt
Width, w (μm)	Initial	100	200	300	100	200	300	100	200	300	200	300
	Final	27	88	151	85	183	180	95	173	178	270	401
Depth, d (μm)	Initial	100	100	100	100	100	100	100	100	100	100	100
	Final	79	49	32	66	31	16	74	40	18	68	58
Aspect ratio = w/d	Initial	1	2	3	1	2	3	1	2	3	2	3
	Final	0.34	1.80	4.72	1.29	5.90	10.63	1.28	4.33	9.89	3.97	6.91

Fig. 12. Changes of stress distributions of the longitudinal surface defects during the single-pass wire drawing.

depth was not noticeable. On the other hand, the surface defect of the blunt cross-section was changed into a shallower shape after the wire drawing because the radial stress component at the bottom was the largest of the three cases. Thus, the bottom of the surface defect was easy to move up in this case during the wire drawing. Finally, the intermediate stress distribution between the sharp and blunt cross-sections was obtained for the medium cross-section, and a similar original shape and aspect ratio were maintained during the wire drawing, even though its width and depth were decreased. Based on these results, it was found that the circumferential and radial stress components during the wire drawing determined the final width and depth of the defect, respectively.

For other types of surface defects, such as transverse, oblique, and round defect, the radial stress components at the bottom of the surface defects were larger than the circumferential components at the top, like the longitudinal defect of the blunt cross-section for all the cases, as shown in Table 5. Therefore, overlapped defects were not observed, regardless of the initial cross-section and direction of the defects.

4.3. Development of the evolution map

Based on the results shown in Fig. 12 and Table 5, stress maps can be derived in terms of the radial stress component at the bottom of the surface defect and the stress ratio ($R = \sigma_{\theta\theta}/\sigma_{rr}$) in Fig. 13. The stress values were calculated with various initial aspect ratios $\varphi = w/d$ (1–3) and angles between the direction of the surface defect and the drawing direction ψ (0–90°). The radial stress component at the bottom increased in comparison with the final depth of the

defect as φ and ψ increased. Similarly, the stress ratio R affecting the final aspect ratio increased as φ and ψ increased.
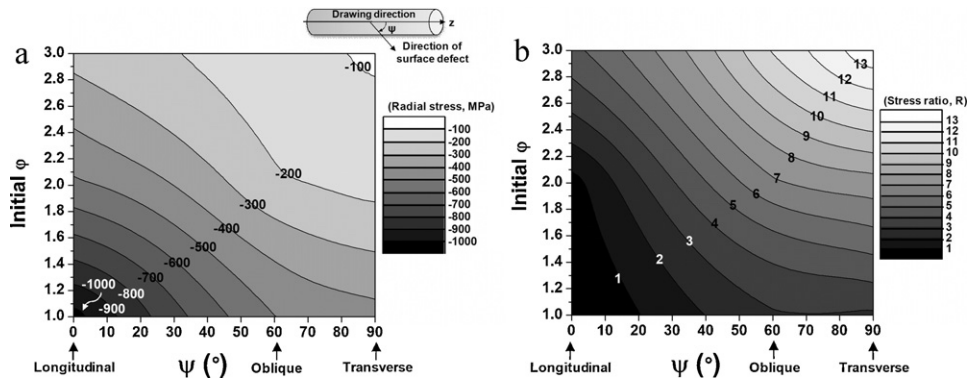
Finally, an evolution map of the surface defect based on the final depth and aspect ratio to set up a guideline to assess the acceptability of the surface defects on the wire is given in Fig. 14. According to this figure, the initial defects formed in the rolling process evolved into either dangerous or safe defects during the single-pass wire drawing based on the final depth and aspect ratio, respectively. As introduced in Section 3.2, the cross-sectional shape of surface defect will be uniquely determined by introducing the aspect ratio φ. The cross-section can be varied while keeping initial cross-sectional shape as a parabola as given in Eq. (3) when its initial aspect ratio varies continuously. In this study, the initial aspect ratio was discretely chosen to be 1, 2, and 3 for three cases of numerical simulations but it can be interpolated to describe the cross-section in the continuous range of initial aspect ratio due to its unique characteristics as mentioned earlier. Since the surface defect cannot be perfectly prevented in the manufacturing process, remaining surface defect of shallow and blunt shape is advantageous for better surface quality of the wire. Therefore, the safest zone was derived as the initial φ and ψ were close to 3 and 90°, respectively, according to the present investigation. The suggested evolution map might be beneficial in screening out the unacceptable surface defects after the wire drawing for commercially available medium carbon steel for practical use.

According to the ASTM Standard (F2282-03, 2009), wire having surface defects shallower than 76 μm can be acceptable due to its surface quality assurance. Therefore, most cases of surface defects investigated in the current numerical simulations were satisfied with the depth criterion of ASTM Standard, except for the

Table 5
Stress components between the top and bottom of the defects during the single-pass wire drawing.

Direction	Longitudinal			Transverse			Oblique			Round	
Cross-section	Sharp	Medium	Blunt	Sharp	Medium	Blunt	Sharp	Medium	Blunt	Medium	Blunt
Radial stress component at the bottom (MPa)	−1038	−520	−268	−437	−169	−89	−502	−218	−139	−425	−297
Circumferential stress component at the top (MPa)	−29	−310	−1259	−1239	−1282	−1239	−1455	−1492	−1552	−1446	−1567

Fig. 13. Stress map of commercially available medium carbon steel in the single-pass wire drawing with various surface defects based on (a) the radial stress component at the bottom of the surface defect and (b) the stress ratio ($R = \sigma_{\theta\theta}/\sigma_{rr}$).
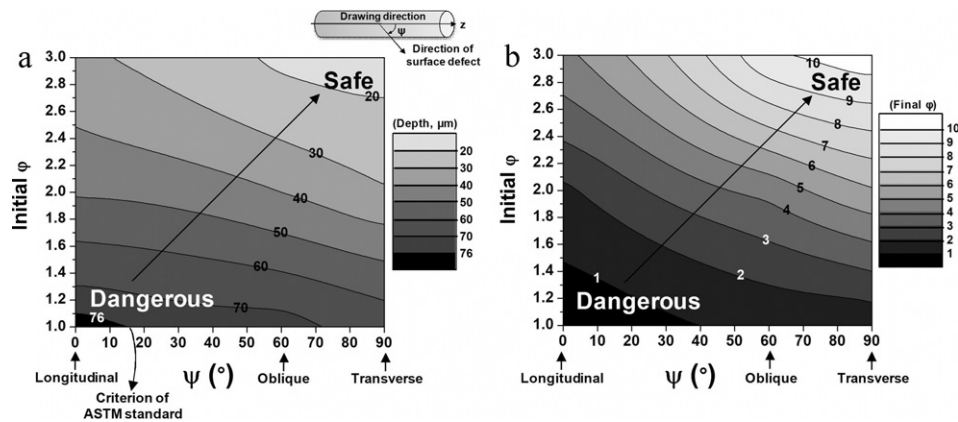
Fig. 14. Evolution map of commercially available medium carbon steel in the single-pass wire drawing with various surface defects based on (a) their final depth and (b) final aspect ratio.

longitudinal surface defect of the sharp cross-section. Therefore, the aspect ratio defined by the ratio of the width to the depth, as introduced in Fig. 2, of equal to or less than 1 for the longitudinal defect should be removed before the secondary forging process or wire drawing for a surface quality assurance criterion, according to the present investigation.

5. Conclusions

In the current study, the deformation behavior of a surface defect with a round shape was investigated using CAMP*form*3D with a free surface contact treatment algorithm for three-dimensional wire drawing simulations. It was found that the numerical simulations matched well with the experimental results for an arbitrary introduced longitudinal surface defect for a multi-pass wire drawing. Therefore, the current numerical approach can be useful for the prediction of the evolution of the surface defects in the wire drawing. Additional numerical simulations were carried out to investigate the deformation behavior of various surface defects possibly formed during the manufacturing processes, such as longitudinal, transverse, oblique, and round defects with various aspect ratios. In the case of longitudinal defects, the initial aspect ratio defined by the ratio of the width to the depth of the defect in the cross-sectional plane was a significant factor determining the final defect shape. For the other cases, however, the aspect ratios decreased to be accepted by the ASTM Standard after the wire drawing, in most cases, under the present investigation conditions. It was found that, for the blunt cross-section, surface defects were easy to cure after the wire drawing process. According to the present investigation, a longitudinal surface defect whose initial aspect ratio was less than one should be properly examined and removed prior to the wire drawing to improve the surface quality of the drawn wire.

The radial and circumferential stress components determined the final shape and aspect ratio of the defect. Finally, an evolution map for the wire drawing of commercially available medium carbon steel was developed to assess the acceptability of the surface quality of the wire for practical use.

Acknowledgments

References

Altan, T., Oh, S.I., Gegel, H.L., 1983. Metal Forming: Fundamentals and Applications, first ed. American Society for Metals, Metals Park, OH.

ASTM Committee E28.042, 2006. E8M-04: Standard Test Methods for Tension Testing of Metallic Materials. ASTM International.

ASTM Committee F16.93., 2009. F2282-03: Standard Specification for Quality Assurance Requirements for Carbon and Alloy Steel Wire, Rods and Bars for Mechanical Fasteners. ASTM International.

Awais, M., Lee, H.W., Im, Y.T., Kwon, H.C., Byon, S.M., Park, H.D., 2008. Plastic work approach for surface defect prediction in the hot bar rolling process. J. Mater. Process. Technol. 201, 73–78.

Chen, C.C., Kobayashi, S., 1978. Deformation analysis of multi-pass bar drawing and extrusion. CIRP Ann. Manuf. Technol. 27, 151–155.

Chevalier, L., 1992. Prediction of defects in metal forming: application to wire drawing. J. Mater. Process. Technol. 32, 145–153.

Hahn, Y.W., Im, Y.T., 1995. Finite element analysis of forming processes with free surface contact algorithm. KSTP Trans. Mater. Process. 4, 48–58 (in Korean).

Huang, H., Gutchess, D., Chang, T., 2004. Imaging-based in-line surface defect inspection for bar rolling. In: Proceedings of the AIST Iron & Steel Conference and Exposition, Nashville, TN, USA, pp. 1–12.

Imiya, T., Kumasaki, T., Nishi, S., Kawaguchi, Y., Marukawa, N., 1981. New system for selective removal of wire rod surface defects. Wire J. Int. 14, 66–77.

Kim, H.Y., Kwon, H.C., Lee, H.W., Im, Y.T., Byon, S.M., Park, H.D., 2008. Processing map approach for surface defect prediction in the hot bar rolling. J. Mater. Process. Technol. 205, 70–80.

Kim, S.Y., Im, Y.T., 2002. Three-dimensional finite element analysis of non-isothermal shape rolling. J. Mater. Process. Technol. 127, 57–63.

Kim, S.Y., Lee, H.W., Min, J.H., Im, Y.T., 2005. Steady state finite element simulation of bar rolling processes based on rigid-viscoplastic approach. Int. J. Numer. Methods Eng. 63, 1583–1603.

Kwak, D.Y., Im, Y.T., 2002. Remeshing for metal forming simulations. Part II. Three-dimensional hexahedral mesh generation. Int. J. Numer. Methods Eng. 53, 2501–2528.

Kwon, H.C., Lee, H.W., Kim, H.Y., Im, Y.T., Park, H.D., Lee, D.L., 2009. Surface wrinkle defect of carbon steel in the hot bar rolling process. J. Mater. Process. Technol. 209, 4476–4483.

Lee, H.W., Kwon, H.C., Awais, M., Im, Y.T., 2007. Instability map based on specific plastic work criterion for hot deformation. J. Mech. Sci. Technol. 21, 1534–1540.

Lee, H.W., Awais, M., Im, Y.T., Lee, Y.H., Son, I.H., Lee, D.L., 2008. Experimental study of surface irregularities of low carbon steel in hot bar rolling. Steel Res. Int. 79, 65–72.

Shinohara, T., Yoshida, K., 2005a. Deformation analysis of surface crack in rolling and wire drawing. JSME Int. J. A 48, 335–340.

Shinohara, T., Yoshida, K., 2005b. Deformation analysis of surface flaws in stainless steel wire drawing. J. Mater. Process. Technol. 162–163, 579–584.

Son, I.H., Lee, J.D., Choi, S., Lee, D.L., Im, Y.T., 2008. Deformation behavior of the surface defects of low carbon steel in wire rod rolling. J. Mater. Process. Technol. 201, 91–96.

Sychkov, A.B., Zhigarev, M.A., Perchatkin, A.V., Mazanov, S.N., Zenin, V.S., 2006. The transformation of defects in continuous-cast semifinished products into surface defects on rolled products. Metallurgist 50, 83–90.

Yoshida, K., Shinohara, T., 2004. Growth and disappearance of flaws on wire surface in wiredrawing. Wire J. Int. 37, 52–57.